Identifying the structure of La₃Ni₂O₇ in the pressurized superconducting state

Hengyuan Zhang,^{1,*} Jielong Zhang,^{1,*} Mengwu Huo,¹ Junfeng Chen,¹ Deyuan Hu,¹ Dao-Xin Yao,¹ Hualei Sun,² Kun Cao,^{1,†} and Meng Wang^{1,‡} Guangdong Provincial Key Laboratory of Magnetoelectric Physics and Devices, School of Physics, Sun Yat-Sen University, Guangzhou, Guangdong 510275, China ² School of Science, Sun Yat-Sen University, Shenzhen, Guangdong 518107, China

The precise crystal structure of $\text{La}_3\text{Ni}_2\text{O}_7$ in its high-pressure superconducting state has been a subject of intense debate, with proposed models including both orthorhombic and tetragonal symmetries. Using high-pressure Raman spectroscopy combined with first-principles calculations, we unravel the structural evolution of $\text{La}_3\text{Ni}_2\text{O}_7$ under pressure up to 32.7 GPa. We identify a clear structural transition sequence: from the orthorhombic Amam phase to a mixed Amam+Fmmm phase at \sim 4 GPa, followed by a complete transition to the tetragonal I4/mmm phase at 14.5 GPa, which is signaled by a pronounced phonon renormalization. The emergence of bulk superconductivity is found to coincide precisely with this transition to the I4/mmm phase. Our results definitively establish the tetragonal I4/mmm structure as the host of superconductivity in $\text{La}_3\text{Ni}_2\text{O}_7$, resolving a central controversy and providing a critical foundation for understanding the superconducting mechanism in nickelates.

Introduction – The discovery of high-temperature superconductivity in Ruddlesden-Popper (RP) nickelates has established a major new family of unconventional superconductors [1, 2]. Superconductivity has been observed in bulk samples of bilayer [3-5], trilayer [6], and hybrid structural phases [7, 8] under high pressure, as well as in thin-film specimens at ambient pressure [9, 10]. Among these, the bilayer compound La₃Ni₂O₇ and its doped derivatives exhibit the highest superconducting transition temperature, T_c [11–13]. This material consists of alternating LaO layers and corner-sharing bilayer NiO₆ octahedra, crystallizing in the orthorhombic Amam space group at ambient pressure [3, 4, 14–17]. A key structural feature is the bilayer of NiO₆ octahedra linked by shared apical oxygen, which is suggested as the fundamental structural unit for superconductivity in RP nickelates [18–27]. In La₃Ni₂O₇, superconductivity emerges above 14 GPa, forming a distinctive right-triangular-like phase diagram [14] that contrasts with the conventional dome-shaped phase diagrams of heavy-fermion systems, cuprates, and iron-based superconductors [28–31]. Identifying the crystal structure in the superconducting state is therefore a crucial first step toward elucidating the underlying mechanism. However, high-pressure constraints and the technical challenges associated with diamond anvil cells (DACs) have hindered structural investigations in this regime. Consequently, the crystallography of La₃Ni₂O₇ in its superconducting state remains a subject of ongoing debate.

Neutron diffraction measurements at ambient pressure confirm an orthorhombic structure for ${\rm La_3Ni_2O_7}$ with a Ni–O–Ni bond angle of 168° along the c axis (Fig. 1a). However, high-pressure structural studies using synchrotron X-ray diffraction (XRD) have yielded conflicting

results, largely due to experimental constraints imposed by the diamond anvil cell (DAC) environment. Three primary structural candidates for the superconducting state have emerged: the unchanged Amam phase [32], an orthorhombic Fmmm phase [3, 14], and a tetragonal I4/mmm phase [15, 16], as shown in Figs. 1a, b. The Fmmm phase, characterized by a 180° Ni-O-Ni bond angle along the c axis, was proposed based on a combination of XRD data and first-principles calculations [3, 4, 14, 17]. In contrast, the I4/mmm phase was identified from Rietveld refinement of XRD patterns in the superconducting state and the merging of the (0 2 0) and (2 0 0) reflection peaks under pressure [15, 16, 33]. The reported pressure for this transition varies, either coinciding with or preceding the emergence of superconductivity, and appears sensitive to the pressure-transmitting medium (PTM) and sample form. Consequently, it remains unclear whether the tetragonal phase is a prerequisite for superconductivity [32]. As a non-destructive optical method, Raman spectroscopy has inherent sensitivity to phonons, making it advantageous for detecting structural symmetry. It has been employed to distinguish the bilayer phase from the other RP nickelates [34] and investigate the electronic correlations in La₄Ni₃O₁₀ at ambient pressure [35–37].

In this work, we investigated the highstructure of La₃Ni₂O₇ by Raman specpressure troscopy. Our results suggest that La₃Ni₂O₇ undergoes three stages of phase transitions: $Amam \xrightarrow{\sim 4 \ GPa} Amam + Fmmm \xrightarrow{14.5 \ GPa} I4/mmm.$ Raman spectra clearly detected a phonon renormalization of La₃Ni₂O₇ at 14.5 GPa, which matches well with our first-principles calculations. The abrupt changes in Raman spectral intensity are attributed to altered phonon vibration patterns accompanying the structural phase transition. More importantly, we identify the structure of La₃Ni₂O₇ in the pressurized superconducting state as belonging to the I4/mmm space group, and resolve the ongoing debates on the correlation of its

^{*} These authors contribute equally to this work.

[†] Corresponding author: caok7@mail.sysu.edu.cn

[‡] Corresponding author: wangmeng5@mail.sysu.edu.cn

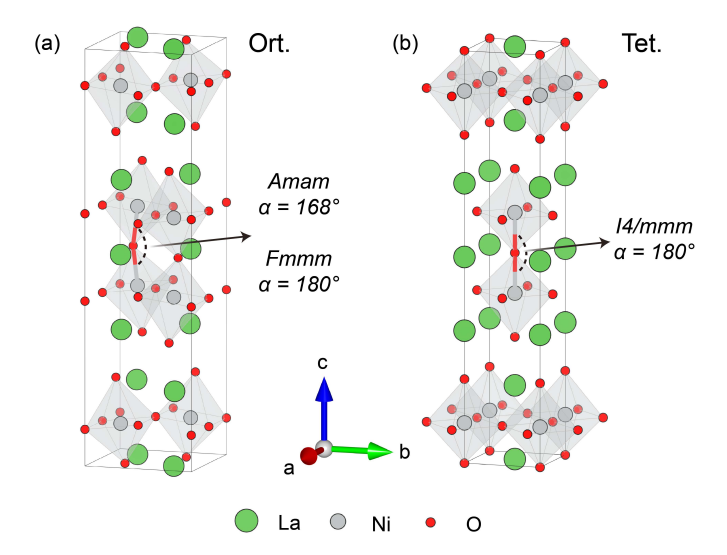


FIG. 1. Crystal structures of $\text{La}_3\text{Ni}_2\text{O}_7$. (a) The low-pressure orthorhombic unit cell (*Amam* or *Fmmm* space groups), characterized by a Ni–O–Ni bond angle of 168° or 180° along the c axis, respectively. (b) The high-pressure tetragonal unit cell (I4/mmm space group).

superconductivity and structural phase transitions.

Experiment and Calculations – Single crystals of La₃Ni₂O₇, grown using a high-pressure optical floating-zone furnace (HKZ, SciDre GmbH), were used in this study [38]. Samples from the same batch were previously characterized in high-pressure electrical transport and XRD experiments [3, 14, 16]. For the present high-pressure Raman measurements, samples were cleaved along the ab-plane and loaded into a DAC. Either neon or helium gas was used as the PTM to ensure a hydrostatic environment. Raman spectra were acquired in a confocal configuration (MoniVista CRS3) using a 633 nm laser as the excitation source, with the power maintained below 3 mW. Low-temperature measurements were performed using an optical magnetic cryostat (Quantum Design), enabling temperature control from 2 to 300 K.

Density functional theory (DFT) calculations were carried out using the Vienna ab initio Simulation Package (VASP) [39, 40]. We employed the Perdew-Burke-Ernzerhof (PBE) functional within the generalized gradient approximation, including onsite Hubbard corrections (PBE+U) [41]. Phonons were computed via density functional perturbation theory in combination with the PHONOPY code. The results were visualized using the VESTA software package [42–44]. Detailed parameters are provided in the Supplemental Material.

Our backscattering Raman experiment, performed with both incident and scattered light polarized in the ab-plane propagating along the c axis, probes Raman activity in the ab-plane, i.e., the derivative of in-plane electric polarizability with respect to phonon modes. Symmetry analysis is performed to provide the forms of Raman tensors for each phase and their corresponding irreducible

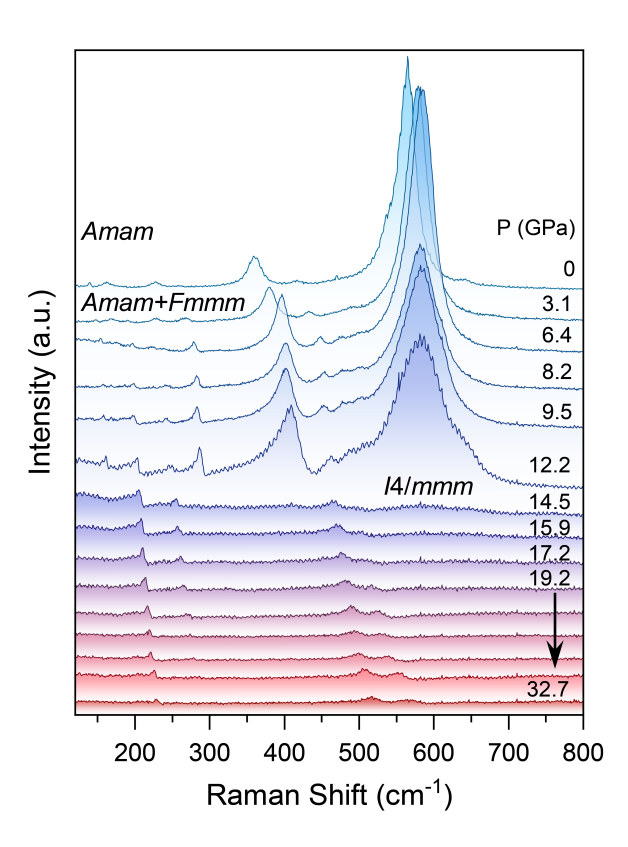


FIG. 2. High-pressure Raman spectra of $\text{La}_3\text{Ni}_2\text{O}_7$. Raman spectra measured from 0 to 32.7 GPa, offset vertically for clarity. At ambient pressure, the spectrum corresponds to the orthorhombic Amam phase. Between 3.1 and 12.2 GPa, the system enters a mixed phase of Amam and Fmmm. Above 14.5 GPa, a transition to the tetragonal I4/mmm phase occurs, accompanied by a reorganization of phonon modes. All spectra were acquired under identical experimental conditions.

representations (ir-reps) (see Section 1 in the supplemental material), with which one can calculate the Raman activity by $I_{ij} \propto \sum_m |\alpha_{ij}|^2$, where i, j = x, y, z denote the polarizations of incident and scattered light respectively, and α_{ij} is the (i,j) th element of the Raman tensor [45]. Therefore, under our experimental setup, only the phonon modes with ir-reps A_g , A_{1g} and B_{1g} will exhibit Raman activity since the others do not possess any nonzero α_{xx} , α_{xy} or α_{yy} elements [46]. Results and Discussions – Raman spectra of a

Results and Discussions – Raman spectra of a La₃Ni₂O₇ single crystal measured within the ab-plane at pressures up to 32.7 GPa are presented in Fig. 2. At ambient pressure, the spectrum for the Amam space group exhibits two primary peaks at 350 cm⁻¹ and 570 cm⁻¹, along with several weaker features, consistent with previous reports [34, 47, 48]. Under increasing pressure, the Raman peaks shift to higher wavenumbers due to lattice compression and broaden progressively, as expected. Above 3.1 GPa, the systematic evolution of the Raman peak at 287 cm⁻¹ signals the onset of a progressive structural transition. A more pronounced transformation occurs at 14.5 GPa and above, where the spectra show a

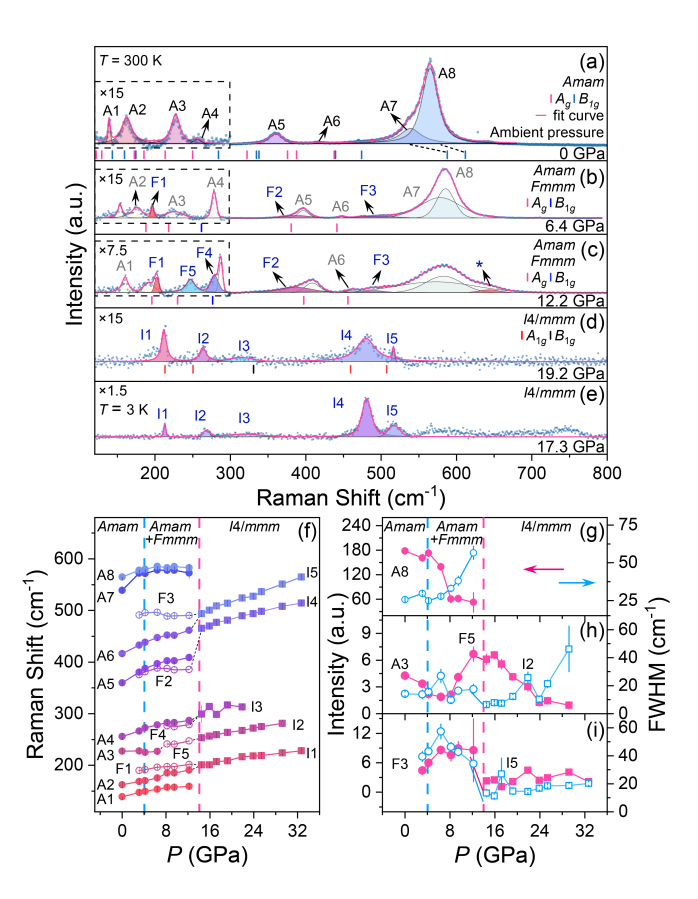


FIG. 3. Raman spectral analysis of La₃Ni₂O₇ under **pressure.** (a) Ambient-pressure spectrum with a linear combination of Lorentzian and Gaussian fits (pink). The phonon modes are deconvoluted into eight peaks (A1-A8), indicated by distinct colored areas. Vertical dashed lines indicate calculated ab-plane phonon frequencies. (b)-(d) Fitted spectra at 6.4, 12.2, and 19.2 GPa (300 K), respectively. Peaks associated with the Fmmm phase (F1-F4) and the I4/mmm phase (I1–I5) are highlighted with colored areas. The vertical lines at the bottom show calculated frequencies for each phase. (e) Spectrum measured at 17.3 GPa and 3 K. For a better visualization, the weak signals in the dashed box were magnified by a factor of (a, b) 15, (c) 7.5. The whole spectra in (d) and (e) were magnified 15 and 1.5, respectively. (f) Pressure dependence of the Raman shifts for all identified phonon modes, labeled according to their respective structural phases: Amam (A1-A8), Fmmm (F1-F4), and I4/mmm (I1-I5). (g)-(i)Pressure evolution of the intensity and full width at half maximum (FWHM) for selected Raman-active phonons.

marked renormalization of phonon modes and the disappearance of the modes at 286, 408, and 582 cm⁻¹, clearly indicating a structural phase transition coincidental with the emergence of superconductivity (See supplementary Fig. S1).

To elucidate the pressure-dependent structural evolution, we compared the experimental Raman spectra measured at selected pressures 0, 6.4, 12.2, and 19.2 GPa (room temperature) with first-principles calculations (Figs. 3a-d). The spectral intensity below $300~\rm cm^{-1}$ is magnified for clarity. At ambient pres-

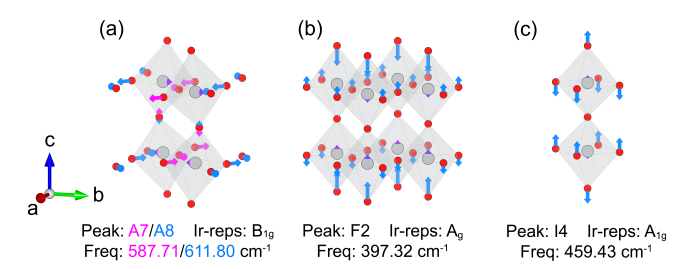


FIG. 4. Visualization of selected phonon mode vibrations. (a) Three-dimensional view of the atomic displacements for phonon modes A7 (magenta arrows) and A8 (azure arrows) in the Amam phase. (b, c) Comparative visualization of a characteristic in-phase vibrational mode in the (b) Fmmm (peak F2) and (c) I4/mmm (peak I4) phases. Atomic displacements are indicated by arrows. For clarity, the illustrations are restricted to the atoms of a single bilayer within the unit cell. The red balls represent O atoms and the grey balls represent Ni atoms. La atoms are omitted as they exhibit negligible displacement in these modes. The corresponding wavenumbers are derived from theoretical calculations.

sure (Fig. 3a), eight phonon modes (labeled A1–A8) are observed, consistent with the calculated A_a and B_{1a} modes of the orthorhombic Amam phase. The reduced number of observed phonon modes compared to calculations is attributed to the Raman spectrometer resolution. At 6.4 GPa, a new peak emerges at 196 cm⁻¹ and the existing peak at 396 cm⁻¹ becomes asymmetric. The spectrum at 12.2 GPa (Fig. 3c) reveals newly emerged peaks (labeled F1-F5) that align with the orthorhombic Fmmm phase, in which the Ni-O-Ni bond angle along the c axis becomes 180° . A broad peak (labeled \star) is also resolved in the fit, which has been interpreted as an indicator of incipient superconductivity at low pressures. The coexistence of Raman peaks at 6.4 and 12.2 GPa indicates a mixed phase of Amam and Fmmm. At 19.2 GPa (Fig. 3d), the phonon modes (labeled I1–I5) match the calculations for the tetragonal I4/mmm phase, characterized by a prominent peak shift to 481 cm⁻¹. Crucially, Raman spectra measured at 3 K in the superconducting state are identical to those at room temperatures, confirming that the structure of superconducting La₃Ni₂O₇ under pressure is the tetragonal I4/mmm phase (Fig. 3e and supplementary Fig. S3).

The dependence of the Raman shifts, intensities, and full width at half maximum (FWHM) on all the applied pressures is detailed in Figs. 3f–i. All observed Raman peaks shift to higher wavenumbers with increasing pressure, consistent with lattice compression. Peaks associated with the Fmmm phase emerge above approximately 4 GPa. In the 4–12 GPa range, the Amam and Fmmm phases coexist, with the relative fraction of the Amam phase decreasing and that of the Fmmm phase increasing gradually, as evidenced by the evolution of peak intensities in Fig. 3g–i. The FWHM of representative modes (A8 and F3) also exhibits anomalies at the structural transition pressures. Above 14 GPa, the Raman spec-

tra undergo an abrupt change due to the transition to the I4/mmm phase, indicative of a first-order structural transition.

To further elucidate the connection between the Raman spectra and structural phase transitions, we identified the relevant phonon modes corresponding to the experimental Raman peaks and plotted their displacement patterns, as shown in Fig. 4. For the primary Raman peak A8 (B_{1g}) in the Amam phase, the associated phonon mode involves vibrations localized on half of the in-plane oxygen atoms within the NiO₆ octahedra (Fig. 4a). These vibrations directly modulate the in-plane bond lengths, resulting in relatively high Raman intensity due to strong coupling with the in-plane polarizability, analogous to a symmetric stretching mode in molecular systems. In contrast, the A7 peak (also B_{1q}) exhibits a similar pattern but is facilitated by the other half of the in-plane oxygen atoms, which are positioned closer to the adjacent layer. Upon transitioning to the Fmmm and I4/mmm phases, where the Ni-O-Ni bond angle along the c axis becomes 180° , the prominent A7 and A8 modes renormalize to form a new vibrational mode. This new mode belongs to the irreducible representations B_{3q} and E_q , respectively (see Supplementary Fig. S5), and is Raman-inactive in our backscattering geometry. Notably, within the Amam space group, the phonon vibration patterns are not sensitive to the tilting angles of the NiO₆ octahedra. Therefore, the emergence of the new Raman peaks F1-F5 at moderate pressures is more likely attributable to the coexistence of the Amam and Fmmm phases, rather than to a continuous pressure-induced change of the Ni–O bond angles within the Amam phase.

Symmetry analysis classifies the F1–F3 and F5 modes as belonging to the A_q irreducible representation, while the I1, I2, I4, and I5 modes belong to A_{1q} ; the remaining F4 and I3 modes are of B_{1g} symmetry. The A_g and A_{1q} modes involve in-phase vibrations of the inplane oxygen atoms along the c axis, modulating both the in-plane and out-of-plane components of the polarizability, as indicated by the non-zero diagonal elements of their Raman tensors (See supplementary Section 3). Figures 4b and c display the in-phase vibrational patterns of modes F2 and I4, which correspond to the Fmmm and I4/mmm phases, respectively. In contrast, the B_{1a} modes are characterized by out-of-phase vibrations of the in-plane oxygen atoms. A notable observation is the significant reduction in Raman intensity for the relatively high-frequency modes (F2-F4) across the transition to the I4/mmm phase. These modes, primarily associated with oxygen atom vibrations, undergo blue shifts during the phase transition, which contributes to the observed intensity suppression [49]. Conversely, the low-frequency modes (F1 and F5), which mainly involve vibrations of La or Ni atoms, exhibit minimal frequency shifts and maintain relatively constant Raman intensities throughout the phase transition.

This Raman spectroscopy study establishes that the

structure of La₃Ni₂O₇ in the pressurized superconducting state is the tetragonal I4/mmm phase, with the emergence of superconductivity coinciding with this structural transition (See supplementary Fig. S1). The apparent discrepancies between high-pressure Raman spectroscopy and synchrotron XRD results can be understood by considering their differing probe depths. Unlike powder samples, single crystals under external pressure develop internal lattice stress, with strain diminishing progressively from the surface to the interior. Our Raman measurements employ a 633 nm laser with an estimated probe depth of \sim 219 nm, whereas a typical synchrotron XRD experiment (wavelength 0.6199 Å) probes the sample with a depth of $\sim 159 \ \mu m$ [50]. For this estimation, we used the absorption coefficient k of LaNiO₃, given its structural similarity to La₃Ni₂O₇. In high-pressure configurations where the sample thickness is typically below 50 μ m, synchrotron radiation probes the volumeaveraged structure, whereas Raman spectroscopy is inherently surface-sensitive, detecting regions where the pressure most closely matches the applied hydrostatic pressure. This gradient in internal lattice stress leads to a distribution of structural states within single crystals. Such inhomogeneity can account for the low superconducting volume fraction observed in single-crystal samples and their pronounced sensitivity to the hydrostaticity of the pressure medium. Furthermore, the welldefined orthorhombic-to-tetragonal transition observed in sol-gel derived powder samples, which lack significant internal stress, provides additional evidence for the presence of substantial strain gradients in single crystals.

Summary - Our high-pressure Raman spectroscopy study, supported by theoretical analysis, elucidates the structural evolution of La₃Ni₂O₇. We identify a clear, multi-stage transition pathway: the ambient-pressure orthorhombic Amam phase first transitions to a mixed phase of Amam and Fmmm at approximately 4 GPa, before undergoing a complete transition to the tetragonal I4/mmm phase at 14.5 GPa. This final transition is marked by a significant renormalization of the phonon spectra. Crucially, the pressure at which superconductivity emerges aligns remarkably with this orthorhombicto-tetragonal structural transition at 14.5 GPa. Our findings therefore definitively identify the tetragonal I4/mmm structure as the crystalline framework for superconductivity in pressurized La₃Ni₂O₇. This result not only resolves a key controversy in the field but also establishes a profound structural parallel with the high- T_c superconducting phases of cuprates and iron-based superconductors, suggesting potentially universal aspects in the lattice environment conducive to unconventional superconductivity.

Acknowledgments—This work was supported by the National Natural Science Foundation of China (Grants No. 12425404, 12494591, 12474137, and 12474249), the National Key Research and Development Program of China (Grants No. 2023YFA1406000, 2023YFA1406500), the Guangdong Basic and Applied Basic Research

Funds (Grant No. 2024B1515020040, 2025B1515020008, 2024A1515030030), the Shenzhen Science and Technology Program (Grants No. RCYX20231211090245050), the Guangzhou Basic and Applied Basic Research Funds (Grant No. 2024A04J6417), the CAS Superconduct-

- ing Research Project (Grant No. SCZX-0101), the Guangdong Provincial Key Laboratory of Magnetoelectric Physics and Devices (Grant No. 2022B1212010008), and Research Center for Magnetoelectric Physics of Guangdong Province (Grant No. 2024B0303390001).
- M. Wang, H. H. Wen, T. Wu, D.-X. Yao, and T. Xiang, Normal and superconducting properties of La₃Ni₂O₇, Chin. Phys. Lett. 41, 077402 (2024).
- [2] Y. Wang, K. Jiang, J. Ying, T. Wu, J. Cheng, J. Hu, and X. Chen, Recent progress in nickelate superconductors, Natl. Sci. Rev., nwaf373 (2025).
- [3] H. Sun, M. Huo, X. Hu, J. Li, Z. Liu, Y. Han, L. Tang, Z. Mao, P. Yang, B. Wang, J. Cheng, D.-X. Yao, G.-M. Zhang, and M. Wang, Signatures of superconductivity near 80 K in a nickelate under high pressure, Nature 621, 493 (2023).
- [4] Y. Zhang, D. Su, Y. Huang, Z. Shan, H. Sun, M. Huo, K. Ye, J. Zhang, Z. Yang, Y. Xu, Y. Su, R. Li, M. Smidman, M. Wang, L. Jiao, and H. Yuan, High-temperature superconductivity with zero resistance and strange-metal behaviour, Nat. Phys. 20, 1269 (2024).
- [5] J. Hou, P.-T. Yang, Z. Y. Liu, J.-Y. Li, P.-F. Shan, L. Ma, G. Wang, N.-N. Wang, H.-Z. Guo, J.-P. Sun, Y. Uwatoko, M. Wang, G.-M. Zhang, B.-S. Wang, and J.-G. Cheng, Emergence of high-temperature superconducting phase in pressurized La₃Ni₂O₇ crystals, Chin. Phys. Lett. 40, 117302 (2023).
- [6] Y. Zhu, D. Peng, E. Zhang, B. Pan, X. Chen, L. Chen, H. Ren, F. Liu, Y. Hao, N. Li, Z. Xing, F. Lan, J. Han, J. Wang, D. Jia, H. Wo, Y. Gu, Y. Gu, L. Ji, W. Wang, H. Gou, Y. Shen, T. Ying, X. Chen, W. Yang, H. Cao, C. Zheng, Q. Zeng, J. G. Guo, and J. Zhao, Superconductivity in pressurized trilayer La₄Ni₃O_{10-δ} single crystals, Nature 631, 531 (2024).
- [7] M. Shi, D. Peng, K. Fan, Z. Xing, S. Yang, Y. Wang, H. Li, R. Wu, M. Du, B. Ge, Z. Zeng, Q. Zeng, J. Ying, T. Wu, and X. Chen, Superconductivity of the hybrid Ruddlesden-Popper La₅Ni₃O₁₁ single crystals under high pressure, arXiv:2502.01018 ().
- [8] C. Huang, J. Li, X. Huang, H. Zhang, D. Hu, M. Huo, X. Chen, Z. Chen, H. Sun, and M. Wang, Superconductivity in monolayer-trilayer phase of La₃Ni₂O₇ under high pressure, arXiv:2510.12250.
- [9] E. K. Ko, Y. Yu, Y. Liu, L. Bhatt, J. Li, V. Thampy, C. T. Kuo, B. Y. Wang, Y. Lee, K. Lee, J. S. Lee, B. H. Goodge, D. A. Muller, and H. Y. Hwang, Signatures of ambient pressure superconductivity in thin film La₃Ni₂O₇, Nature 638, 935 (2025).
- [10] G. Zhou, W. Lv, H. Wang, Z. Nie, Y. Chen, Y. Li, H. Huang, W.-Q. Chen, Y.-J. Sun, Q.-K. Xue, and Z. Chen, Ambient-pressure superconductivity onset above 40 K in (La,Pr)₃Ni₂O₇ films, Nature 640, 641 (2025).
- [11] F. Li, Z. Xing, D. Peng, J. Dou, N. Guo, L. Ma, Y. Zhang, L. Wang, J. Luo, J. Yang, J. Zhang, T. Chang, Y.-S. Chen, W. Cai, J. Cheng, Y. Wang, Z. Zeng, Q. Zheng, R. Zhou, Q. Zeng, X. Tao, and J. Zhang, Ambient pressure growth of bilayer nickelate single crystals with superconductivity over 90 K under high pressure,

- arXiV:2501.14584.
- [12] Q. Zhong, J. Chen, Z. Qiu, J. Li, X. Huang, P. Ma, M. Huo, H. Dong, H. Sun, and M. Wang, Evolution of the superconductivity in pressurized La_{3-x}Sm_xNi₂O₇, arXiv:2510.13342.
- [13] Z. Qiu, J. Chen, D. V. Semenok, Q. Zhong, D. Zhou, J. Li, P. Ma, X. Huang, M. Huo, T. Xie, X. Chen, H. kwang Mao, V. Struzhkin, H. Sun, and M. Wang, Interlayer coupling enhanced superconductivity near 100 K in $\text{La}_{3-x}\text{Nd}_x\text{Ni}_2\text{O}_7$, arXiv:2510.12359.
- [14] J. Li, D. Peng, P. Ma, H. Zhang, Z. Xing, X. Huang, C. Huang, M. Huo, D. Hu, Z. Dong, X. Chen, T. Xie, H. Dong, H. Sun, Q. Zeng, H.-k. Mao, and M. Wang, Identification of superconductivity in bilayer nickelate La₃Ni₂O₇ under high pressure up to 100 GPa, Natl. Sci. Rev., nwaf220 (2025).
- [15] G. Wang, N. Wang, T. Lu, S. Calder, J. Yan, L. Shi, J. Hou, L. Ma, L. Zhang, J. Sun, B. Wang, S. Meng, M. Liu, and J. Cheng, Chemical versus physical pressure effects on the structure transition of bilayer nickelates, npj Quantum Mater. 10, 1 (2025).
- [16] L. Wang, Y. Li, S. Y. Xie, F. Liu, H. Sun, C. Huang, Y. Gao, T. Nakagawa, B. Fu, B. Dong, Z. Cao, R. Yu, S. I. Kawaguchi, H. Kadobayashi, M. Wang, C. Jin, H. K. Mao, and H. Liu, Structure responsible for the superconducting state in La₃Ni₂O₇ at high-pressure and lowtemperature conditions, J. Am. Chem. Soc. 146, 7506 (2024).
- [17] M. Zhang, C. Pei, Q. Wang, Y. Zhao, C. Li, W. Cao, S. Zhu, J. Wu, and Y. Qi, Effects of pressure and doping on Ruddlesden-Popper phases La_{n+1}Ni_nO_{3n+1}, J. Mater. Sci. Technol. 185, 147 (2024).
- [18] Z. Luo, X. Hu, M. Wang, W. Wú, and D.-X. Yao, Bilayer two-orbital model of La₃Ni₂O₇ under pressure, Phys. Rev. Lett. 131, 126001 (2023).
- [19] J. Yang, H. Sun, X. Hu, Y. Xie, T. Miao, H. Luo, H. Chen, B. Liang, W. Zhu, G. Qu, C.-Q. Chen, M. Huo, Y. Huang, S. Zhang, F. Zhang, F. Yang, Z. Wang, Q. Peng, H. Mao, G. Liu, Z. Xu, T. Qian, D.-X. Yao, M. Wang, L. Zhao, and X. J. Zhou, Orbital-dependent electron correlation in double-layer nickelate La₃Ni₂O₇, Nat. Commun. 15, 4373 (2024).
- [20] Z. Liu, M. Huo, J. Li, Q. Li, Y. Liu, Y. Dai, X. Zhou, J. Hao, Y. Lu, M. Wang, and H.-H. Wen, Electronic correlations and partial gap in the bilayer nickelate La₃Ni₂O₇, Nat. Commun. 15, 7570 (2024).
- [21] X.-Z. Qu, D.-W. Qu, J. Chen, C. Wu, F. Yang, W. Li, and G. Su, Bilayer $t J J_{\perp}$ model and magnetically mediated pairing in the pressurized nickelate La₃Ni₂O₇, Phys. Rev. Lett. **132**, 036502 (2024).
- [22] C. Lu, Z. Pan, F. Yang, and C. Wu, Interlayer-coupling-driven high-temperature superconductivity in La₃Ni₂O₇ under pressure, Phys. Rev. Lett. 132, 146002 (2024).
- [23] H. Sakakibara, N. Kitamine, M. Ochi, and K. Kuroki,

- Possible high T_c superconductivity in La₃Ni₂O₇ under high pressure through manifestation of a nearly half-filled bilayer Hubbard model, Phys. Rev. Lett. **132**, 106002 (2024).
- [24] Y. Zhang, L.-F. Lin, A. Moreo, T. A. Maier, and E. Dagotto, Structural phase transition, s_±-wave pairing, and magnetic stripe order in bilayered superconductor La₃Ni₂O₇ under pressure, Nat. Commun. 15, 2470 (2024).
- [25] K.-Y. Jiang, Y.-H. Cao, Q.-G. Yang, H.-Y. Lu, and Q.-H. Wang, Theory of pressure dependence of superconductivity in bilayer nickelate La₃Ni₂O₇, Phys. Rev. Lett. 134, 76001 (2025).
- [26] Y.-f. Yang, G.-M. Zhang, and F.-C. Zhang, Interlayer valence bonds and two-component theory for high-T_c superconductivity of La₃Ni₂O₇ under pressure, Phys. Rev. B 108, L201108 (2023).
- [27] F. Lechermann, J. Gondolf, S. Bötzel, and I. M. Eremin, Electronic correlations and superconducting instability in La₃Ni₂O₇ under high pressure, Phys. Rev. B 108, L201121 (2023).
- [28] M. K. Crawford, R. L. Harlow, S. Deemyad, V. Tissen, J. S. Schilling, E. M. Mccarron, S. W. Tozer, D. E. Cox, N. Ichikawa, and S. Uchida, High-pressure study of structural phase transitions and superconductivity in La_{1.48}Nd_{0.4}Sr_{0.12}CuO₄, Phys. Rev. B 71, 104513 (2005).
- [29] J. B. Zhang, V. V. Struzhkin, W. Yang, H. K. Mao, H. Q. Lin, Y. C. Ma, N. L. Wang, and X. J. Chen, Effects of pressure and distortion on superconductivity in Tl₂Ba₂CaCu₂O_{8+δ}, Journal of Physics:Condensed Matter 27, 445701 (2015).
- [30] Massidda, Sandro, Martinelli, Alberto, Bernardini, and Fabio, The phase diagrams of iron-based superconductors: Theory and experiments, Comptes Rendus Physique 17, 5 (2016).
- [31] S. Medvedev, T. M. Mcqueen, and I. A. Troyan, Electronic and magnetic phase diagram of β -Fe_{1.01}Se with superconductivity at 36.7 K under pressure, Nature materials 8, 630 (2009).
- [32] M. Shi, D. Peng, Y. Li, Z. Xing, Y. Wang, K. Fan, H. Li, R. Wu, Z. Zeng, Q. Zeng, J. Ying, T. Wu, and X. Chen, Prerequisite of superconductivity: SDW rather than tetragonal structure in double-layer ${\rm La_3Ni_2O_{7-x}}$, ${\rm arXiv:2501.14202}$ ().
- [33] P. Puphal, P. Reiss, N. Enderlein, Y.-M. Wu, G. Khaliullin, V. Sundaramurthy, T. Priessnitz, M. Knauft, A. Suthar, L. Richter, M. Isobe, P. A. Van Aken, H. Takagi, B. Keimer, Y. E. Suyolcu, B. Wehinger, P. Hansmann, and M. Hepting, Unconventional crystal structure of the high-pressure superconductor La₃Ni₂O₇, Phys. Rev. Lett. 133, 146002 (2024).
- [34] Y. Li, Y. Cao, L. Liu, P. Peng, H. Lin, C. Pei, M. Zhang, H. Wu, X. Du, W. Zhao, K. Zhai, X. Zhang, J. Zhao, M. Lin, P. Tan, Y. Qi, G. Li, H. Guo, L. Yang, and L. Yang, Distinct ultrafast dynamics of bilayer and trilayer nickelate superconductors regarding the densitywave-like transitions, Sci. Bull. 70, 180 (2025).
- [35] A. Suthar, V. Sundaramurthy, M. Bejas, C. Le, P. Puphal, P. Sosa-Lizama, A. Schulz, J. Nuss, M. Isobe, P. A. van Aken, Y. E. Suyolcu, M. Minola, A. P. Schnyder, X. Wu, B. Keimer, G. Khaliullin, A. Greco, and

- M. Hepting, Multiorbital character of the density wave instability in $La_4Ni_3O_{10}$, arXiv:2508.06440.
- [36] D.-H. Gim, C. H. Park, and K. H. Kim, Orbital-selective quasiparticle depletion across the density wave transition in trilayer nickelate La₄Ni₃O₁₀, Phys. Rev. Lett. 135, 136505 (2025).
- [37] S. Zhang, H. Zhang, Z. Dong, J. Li, Q. Xiao, M. Huo, H.-Y. Huang, D.-J. Huang, Y. Wang, Y. Lu, Z. Chen, M. Wang, and Y. Peng, Distinct orbital contributions to electronic and magnetic structures in La₄Ni₃O₁₀, arXiv:2509.20727.
- [38] Z. Liu, H. Sun, M. Huo, X. Ma, Y. Ji, E. Yi, L. Li, H. Liu, J. Yu, Z. Zhang, Z. Chen, F. Liang, H. Dong, H. Guo, D. Zhong, B. Shen, S. Li, and M. Wang, Evidence for charge and spin density waves in single crystals of La₃Ni₂O₇ and La₃Ni₂O₆, Sci. China-Phys. Mech. Astron. 66, 217411 (2023).
- [39] G. Kresse and J. Hafner, Ab initio molecular dynamics for liquid metals, Phys. Rev. B 47, 558 (1993).
- [40] G. Kresse and J. Furthmüller, Efficient iterative schemes for ab initio total-energy calculations using a plane-wave basis set, Phys. Rev. B 54, 11169 (1996).
- [41] J. P. Perdew, K. Burke, and M. Ernzerhof, Generalized gradient approximation made simple, Phys. Rev. Lett. 77, 3865 (1996).
- [42] A. Togo, L. Chaput, T. Tadano, and I. Tanaka, Implementation strategies in phonopy and phono3py, J. Phys. Condens. Matter 35, 353001 (2023).
- [43] A. Togo, First-principles phonon calculations with phonopy and phono3py, J. Phys. Soc. Jpn. 92, 012001 (2023).
- [44] K. Momma and F. Izumi, VESTA3 for three-dimensional visualization of crystal, volumetric and morphology data, Journal of Applied Crystallography 44, 1272 (2011).
- [45] D. Porezag and M. R. Pederson, Infrared intensities and raman-scattering activities within density-functional theory, Phys. Rev. B 54, 7830 (1996).
- [46] X. Zhang, X.-F. Qiao, W. Shi, J.-B. Wu, D.-S. Jiang, and P.-H. Tan, Phonon and raman scattering of twodimensional transition metal dichalcogenides from monolayer, multilayer to bulk material, Chem. Soc. Rev. 44, 2757 (2015).
- [47] J. Wen, Y. Xu, G. Wang, Z.-X. He, Y. Chen, N. Wang, T. Lu, X. Ma, F. Jin, L. Chen, M. Liu, J.-W. Fan, X. Liu, X. Yu Pan, G.-Q. Liu, J. Cheng, and X. Yu, Imaging the Meissner effect in pressurized bilayer nickelate with integrated multi-parameter quantum sensor, Natl. Sci. Rev., nwaf268 (2025).
- [48] Y. Meng, Y. Yang, H. Sun, S. Zhang, J. Luo, L. Chen, X. Ma, M. Wang, F. Hong, X. Wang, and X. Yu, Densitywave-like gap evolution in La₃Ni₂O₇ under high pressure revealed by ultrafast optical spectroscopy, Nat. Commun. 15, 10408 (2024).
- [49] W. Holzer, W. Murphy, and H. Bernstein, Raman spectra of negative molecular ions doped in alkali halide crystals, Journal of Molecular Spectroscopy 32, 13 (1969).
- [50] P. Borowicz, Depth-sensitive raman investigation of metal-oxide-semiconductor structures: Absorption as a tool for variation of exciting light penetration depth, Journal of Spectroscopy 2016, 1617063 (2016).

Supplementary: Identifying the structure of La₃Ni₂O₇ in the pressurized superconducting state

Hengyuan Zhang,^{1,*} Jielong Zhang,^{1,*} Mengwu Huo,¹ Junfeng Chen,¹ Deyuan Hu,¹ Dao-Xin Yao,¹ Hualei Sun,² Kun Cao,^{1,†} and Meng Wang^{1,‡} ¹ Guangdong Provincial Key Laboratory of Magnetoelectric Physics and Devices, School of Physics, Sun Yat-Sen University, Guangzhou, Guangdong 510275, China ² School of Science, Sun Yat-Sen University, Shenzhen, Guangdong 518107, China

Section 1. Details of the experiments

A. $La_3Ni_2O_7$ single crystals growth

Single crystals of La₃Ni₂O₇ were grown using a highpressure optical floating zone furnace (model HKZ, SciDre GmbH). The precursor polycrystalline were synthesized by solid-state method. The starting materials of La₂O₃ were dried at 1000 °C for 12 hours before use. Stoichiometric amounts of La₂O₃ and NiO were mixed and sintered at 1200 °C for 1 day. Subsequently, the powders were pressed into rods with 6 mm in diameter and 100 mm in length under a hydrostatic pressure and then heated at 1200 °C for 48 hours. Single crystals La₃Ni₂O₇ were grown by the floating zone method at a rate of 4 mm/h in flowing O₂ atmosphere at a pressure of 20 bar and 15 bar, respectively.

B. High-pressure electric transport measurements

We performed electrical transport measurements on La₃Ni₂O₇ crystals under high pressure by using a miniature diamond anvil cell (DAC) constructed from a Be-Cu alloy. The DAC utilized diamond anvils with culets about 300 μ m and an insulating gasket chamber, 100 μ m in diameter, composed of a cubic boron nitride and epoxy mixture. The four-probe van der Pauw technique was applied for the electrical measurements, which were executed with the KBr as a pressure-transmitting medium (PTM). The high-pressure resistance of a La₃Ni₂O₇ single crystal from 8.8 GPa to 18.9 GPa, as shown in Fig. S1.

C. High-pressure Raman experiments

Prior to the Raman measurements, we performed a Laue diffraction experiment on the sample to verify that the incident Raman light was perpendicular to the *ab*-plane, as illustrated in Fig. S2.

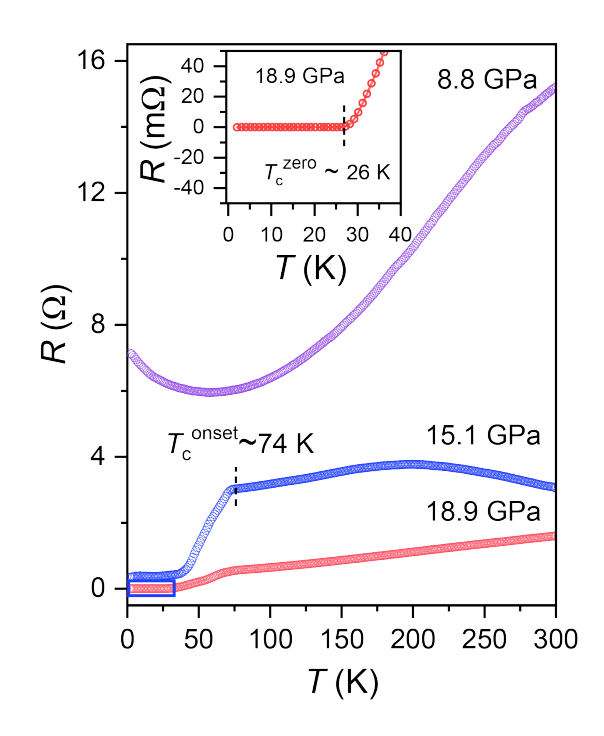


FIG. S1. The high-pressure resistance curves of La₃Ni₂O₇ single crystals from 8.8 GPa to 18.9 GPa. T_c^{onset} and T_c^{zero} are respectively defined as the onset SC transition temperature and zero resistance temperature. T_c^{onset} =74 K is observed at 15.1 GPa. The inset clearly shows the $T_c^{zero} \sim 26$ K at 18.9 GPa, which means that high-quality La₃Ni₂O₇ superconducting single crystals have been synthesized.

High pressure was generated using a symmetric diamond anvil cell (DAC) with 300 μm culet. A rhenium gasket with the central 200 μm hole drilled by laser milling was used as the sample chamber. Hyperbaric Ne gas or He gas was fed into the sample chamber as the pressure transmission medium to keep hydrostatic pressure environment. After pressurization and sealing, the hole diameter shrank to approximately 100 μm .

The Raman spectrum was acquired using a confocal geometry (MoniVist a CRS3) equipped with the Princeton Instrument HRS-500 spectrometer and 633 nm laser as the excitation source. A grating with 1200 g/mm was used to achieve high energy resolution for the phonon lines, providing an energy resolution of 1.5 cm⁻¹. The laser power was controlled below 3 mW to minimize the heating effect. A \times 20 objective lens (Zeiss, 0.25 NA) was used to focus the laser beam onto the sample and

^{*} These authors contribute equally to this work.

 $^{^\}dagger$ Corresponding author: caok 7@mail.sysu.edu.cn

[‡] Corresponding author: wangmeng5@mail.sysu.edu.cn

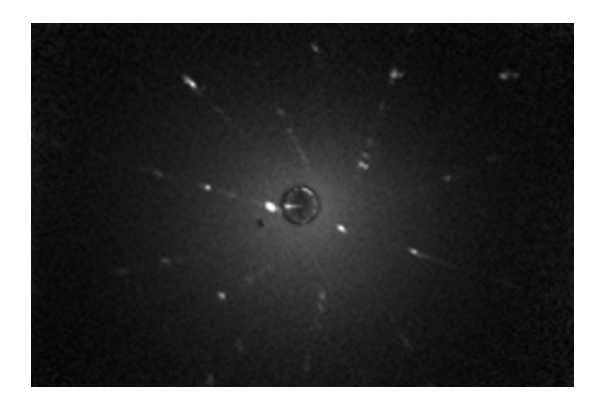


FIG. S2. Laue X-ray diffraction for La₃Ni₂O₇.

to collect the scattered light (back scattering geometry). The spectrometer was equipped with a nitrogen-cooled CCD detector. The DAC was placed on the thermal conduction stage of an Optical Magnetic Cryostat (Quantum Design) to enable temperature control from 2-300 K. Resistive temperature sensor (Cernox, Quantum Design) was attached near the sample chamber to measure temperature. The thermometer covers a range from 0.1 K to 420 K, meeting the experiment's required measurement precision. The optical observation window of the Optical Magnetic Cryostat can be coupled to the Raman apparatus to perform low-temperature Raman measurements. Temperature-dependent Raman spectra of La₃Ni₂O₇ at 5 GPa and 17 GPa are provided in Fig. S3. Notably, no polarizer or analyzer was inserted into the optical path. Therefore, the unpolarized Raman spectrum includes information from all polarization channels. The L+G(Lorentzian with Gaussian) function was used to describe the phonon lines. For the temperature-dependent spectra, the Bose-Einstein factor is divided for comparison.

In all high-pressure experiments, the pressure was jointly monitored by ruby fluorescence (0-15 GPa) and high-frequency edge of the diamond phonon (above 10 GPa).

Section 2. The effective detection depth for Raman and Synchrotron XRD

D. The effective detection depth for Raman

Since the theoretical expressions for the effective probing depth of Raman scattering are already reported in the literature [1], we only present here the primary formulas and the derivation of the effective depth specifically for ${\rm La_3Ni_2O_7}$.

The absorption of material is described by Lambert law:

$$I(l) = I_0 e^{-\alpha l} \tag{1}$$

where I_0 denotes the intensity of incident light, l is the optical pathway through the material, I(l) is the intensity

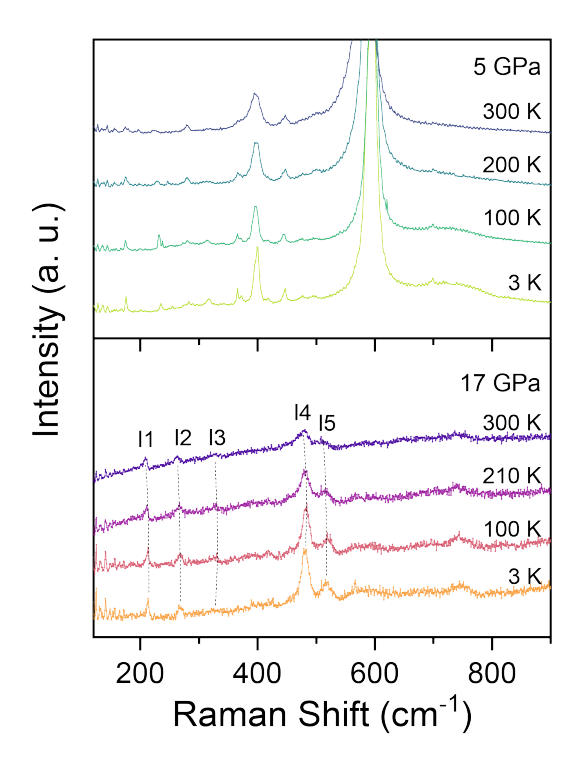


FIG. S3. Temperature-dependent Raman spectra of $La_3Ni_2O_7$ at 5 GPa and 17 GPa.

of the light after the pathway equal to l, and α is the absorption coefficient of the material. α can be expressed as a function of imaginary parts of complex refractive index k (or be called damping coefficient) by following equation:

$$\alpha = \frac{4\pi k}{\lambda} \tag{2}$$

where k denote imaginary parts of complex refractive index, is functions of wavelength λ . Penetration depth δ is defined as thickness of absorbing material which corresponds to the decrease of the quantity describing electromagnetic wave by e times—— in Eq.(1), $\alpha l=1$. So, the δ can be described as:

$$\delta = \frac{\lambda}{4\pi k} = \alpha^{-1} \tag{3}$$

Integrate the intensity of scattered light I(l) over the material thickness l to obtain the total scattering intensity.:

$$I(l) = I_0 \varphi_0 \int_0^l e^{-2\alpha z} dz = I_0 \varphi_0 \frac{1 - e^{-2\alpha l}}{2\alpha}.$$
 (4)

In Eq. (4) I_0 denotes the intensity of excitation and φ_0 describes the efficiency of the observed Raman effect. Integration from 0 to l gives the intensity of Raman scattering measured from the layer whose thickness is equal to l. The expression $e^{-2\alpha z}$ under the integral described the statistical weight of the contribution of the scattering coming from the material placed at the depth equal to z.

Factor 2 in the argument of exponential function in Eq. (4) was introduced because scattered light is absorbed in the same manner as exciting light. If $l \to \infty$, we can get $I_{max} = I_0 \varphi_0 \frac{1}{2\alpha}$. For a fixed material (k known), once the λ is set, the material's δ is fixed. For now, assume that the effective probing depth $\delta_{\rm eff}^{\rm max} = n\delta$, we can estimate the value of n:

$$\frac{I(n\delta)}{I_{max}} = \frac{I_0 \varphi_0 \frac{1 - e^{-2\alpha(n\delta)}}{2\alpha}}{I_0 \varphi_0 \frac{1}{2\alpha}} = 1 - e^{-2\alpha(n\delta)} = 1 - e^{-2n}. (5)$$

when n=3, $\frac{I(3\delta)}{I_{max}}\approx 0.9975$. Further increasing depth results in a signal gain that is smaller than the statistical error of a typical CCD detector (approximately 0.004). So, when we know the δ , we can estimate the $\delta_{\rm eff}^{\rm max}=3\delta$. Therefore, assuming the absorption coefficient k is known, we determine the material's effective detection depth $\delta_{\rm eff}^{\rm max}$. Since the k for La₃Ni₂O₇ is unknown, while the k for La₁NiO₃ has been reported (k=0.69)[2]. The La₁NiO₃ and La₃Ni₂O₇ share the same chemical elements and have similar chemical densities. Therefore we use the k of La₁NiO₃ to replace that of La₃Ni₂O₇. In our experiment, k=633 nm. According to the Eq.(3), we can get the k (k=0.69) k=0.69 nm. In actual experiments, the effective detection depth of k=0.69 nm. In actual experiments, the effective detection depth of k=0.69 nm. In actual experiments, the effective detection depth of k=0.69 nm.

E. The effective detection depth for Synchrotron XRD

For synchrotron XRD, the attenuation of light intensity with depth still follows the Lambert-Beer law. However, for high-energy X-rays, the interaction with matter is dominated by the photoelectric effect. Therefore, the absorption capability of matter for X-rays should be described using the linear attenuation coefficient rather than the imaginary part of the complex refractive index:

$$I(l) = I_0 e^{-\mu l} \tag{6}$$

 μ is linear attenuation coefficient of material. The δ is defined as the depth at which the X-ray intensity has decayed to 1/e of the surface intensity; the formula for this is:

$$\delta = \frac{1}{\mu} \tag{7}$$

The linear absorption coefficient μ is determined by the material's mass absorption coefficient μ_m and its density ρ :

$$\mu = \rho \times \mu_m \tag{8}$$

Consider a simple semi-infinite bulk sample. An X-ray beam strikes the sample at an incident angle θ_i . At a certain depth z within the sample, Bragg diffraction occurs

on a crystal plane (with a diffraction angle of θ_d). The diffracted X-ray then exits the surface of the sample at the same angle θ_d . We can calculated the incident path l_i : $\frac{z}{sin\theta_i}$, emergent path l_d : $\frac{z}{sin\theta_d}$. The total diffraction intensity is the sum (integral) of contributions from all depths z:

$$I_{diff} = \int_{0}^{l} dI_{diff} = CI_{0} \int_{0}^{l} e^{-\mu z (\frac{1}{\sin \theta_{i}} + \frac{1}{\sin \theta_{d}})} dz$$

$$= CI_{0} \frac{1 - e^{-\mu l (\frac{1}{\sin \theta_{i}} + \frac{1}{\sin \theta_{d}})}}{\mu (\frac{1}{\sin \theta_{i}} + \frac{1}{\sin \theta_{d}})}$$
(9)

C represents the inherent diffraction capability of this material. If $l \to \infty$, the Eq.(9) is:

$$I_{max \cdot diff} = \frac{CI_0}{\mu(\frac{1}{\sin \theta_i} + \frac{1}{\sin \theta_d})}$$
 (10)

We can still make an approximation similar to that in Eq(5):

$$\frac{I(n\delta)_{diff}}{I_{max \cdot diff}} = \frac{CI_0 \frac{1 - e^{-\mu(n\delta)(\frac{1}{\sin\theta_i} + \frac{1}{\sin\theta_d})}}{\mu(\frac{1}{\sin\theta_i} + \frac{1}{\sin\theta_d})}}{CI_0 \frac{1}{\mu(\frac{1}{\sin\theta_i} + \frac{1}{\sin\theta_i})}}$$

$$= 1 - e^{-\mu(n\delta)(\frac{1}{\sin\theta_i} + \frac{1}{\sin\theta_d})}$$

$$= 1 - e^{-2n}$$
(11)

We assume symmetric diffraction in Eq. (11), and $\theta_i = \theta_d = 90^{\circ}$. The result of Eq. (11) is same as that of Eq. (5), so n = 3. For now, we can derive the maximum detection depth of La₃Ni₂O₇ in synchrotron XRD. For the mass absorption coefficient of composites μ_m , we can compute a weighted average using each component's mass fraction w_i and its own mass absorption coefficient $\mu_{m,i}$:

$$\mu_m = \sum_i w_i \times \mu_{m,i} \tag{12}$$

Given wavelength $\lambda=0.6199$ Å (The wavelength come from the BL15U1 beamline of the Shanghai Synchrotron Radiation Facility (SSRF)), the corresponding photon energy $E\approx 20.00$ keV. The molar mass of $M(La_3Ni_2O_7)$ is 646.11g/mol. At 20 keV, the mass attenuation coefficients μ_m for each element [3] are: $\mu_{m,La}=36.44$ cm²/g, $\mu_{m,Ni}=16.56$ cm²/g, $\mu_{m,O}=0.738$ cm²/g. The mass absorption coefficient μ_m of La₃Ni₂O₇ is calculated as:

$$\mu_m = w_{\text{La}} \times \mu_{m,\text{La}} + w_{\text{Ni}} \times \mu_{m,\text{Ni}} + w_{\text{O}} \times \mu_{m,\text{O}}$$

$$= 0.6450 \times 36.44 + 0.1817 \times 16.56 + 0.1733 \times 0.738$$

$$\approx 26.64 \text{ cm}^2/\text{g}$$
(13)

La₃Ni₂O₇ has a density of approximately $\rho = 7.1 \ g/cm^3$, and the linear absorption coefficient μ is calculated as:

$$\mu = \rho \times \mu_m = 7.1 \times 26.64 \approx 189.14 \text{ cm}^{-1}$$
 (14)

So, the δ is μ^{-1} :

$$\delta = \frac{1}{\mu} = \frac{1}{189.14} \approx 0.00529 \text{ cm} = 52.9 \ \mu\text{m}$$
 (15)

$$\delta_{max \cdot diff} = 3 \times \delta = 158.6 \ \mu \text{m} \tag{16}$$

It is evident that Raman has an effective detection depth that differs from synchrotron XRD by roughly three orders of magnitude. In high-pressure experiments, where sample thickness is usually less than 50 μ m. So, synchrotron radiation probes the bulk phase, whereas Raman spectroscopy tends to be more sensitive to surface information.

Section 3. Details of the calculations

F. Detailed calculation parameters

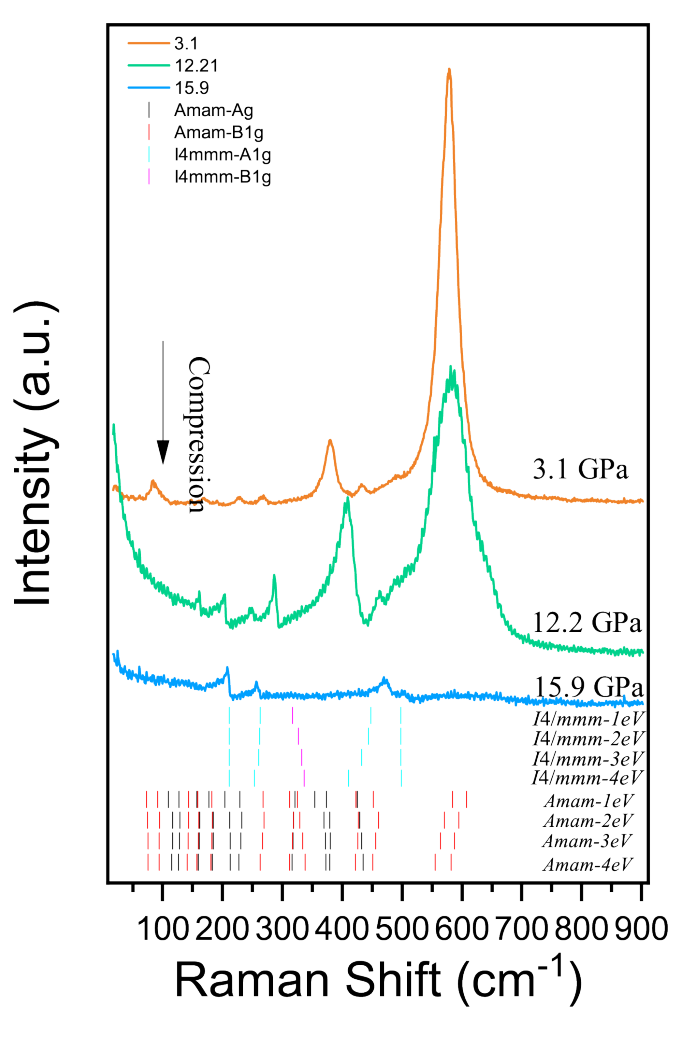


FIG. S4. Calculated frequencies of Raman active modes with different Hubbard U.

The projector augmented-wave (PAW) method[4] with a kinetic energy cutoff of 500 eV was employed. A $6\times6\times6$ and a $9\times9\times9$ (for Fmmm and I4/mmm) Monkhorst-Pack k-point mesh were used for the Amam and for the Fmmm and I4/mmm phase, respectively. The effective Hubbard U parameter was set to 1 eV (Fig. S4). Atomic positions were relaxed until the atomic forces converged less than 10^{-2} eV/Å.

G. Raman tensors

The Raman tensors are given as[5]:

$$R_{Amam}: egin{pmatrix} a & 0 & 0 \ 0 & b & 0 \ 0 & 0 & c \end{pmatrix}_{A_a}, egin{pmatrix} 0 & d & 0 \ d & 0 & 0 \ 0 & 0 & 0 \end{pmatrix}_{B_{1a}},$$

$$\begin{pmatrix} 0 & 0 & e \\ 0 & 0 & 0 \\ e & 0 & 0 \end{pmatrix}_{B_{2q}}, \begin{pmatrix} 0 & 0 & 0 \\ 0 & 0 & f \\ 0 & f & 0 \end{pmatrix}_{B_{3q}},$$

$$R_{Fmmm}: \begin{pmatrix} a & 0 & 0 \\ 0 & b & 0 \\ 0 & 0 & c \end{pmatrix}_{A_g}, \begin{pmatrix} 0 & d & 0 \\ d & 0 & 0 \\ 0 & 0 & 0 \end{pmatrix}_{B_{1g}},$$

$$\begin{pmatrix} 0 & 0 & e \\ 0 & 0 & 0 \\ e & 0 & 0 \end{pmatrix}_{B_{2q}}, \begin{pmatrix} 0 & 0 & 0 \\ 0 & 0 & f \\ 0 & f & 0 \end{pmatrix}_{B_{3q}},$$

$$R_{I4/mmm}: \begin{pmatrix} a & 0 & 0 \\ 0 & a & 0 \\ 0 & 0 & b \end{pmatrix}_{A_{1a}}, \begin{pmatrix} c & 0 & 0 \\ 0 & -c & 0 \\ 0 & 0 & 0 \end{pmatrix}_{B_{1a}},$$

$$\begin{pmatrix} 0 & d & 0 \\ d & 0 & 0 \\ 0 & 0 & 0 \end{pmatrix}_{B_{2g}}, \begin{pmatrix} 0 & 0 & 0 \\ 0 & 0 & e \\ 0 & e & 0 \end{pmatrix}_{E_g}, \begin{pmatrix} 0 & 0 & e \\ 0 & 0 & 0 \\ -e & 0 & 0 \end{pmatrix}_{E_g},$$

where, in general, the parameters a, b, c, d, e and f are distinct for each phase.

H. Additional figures

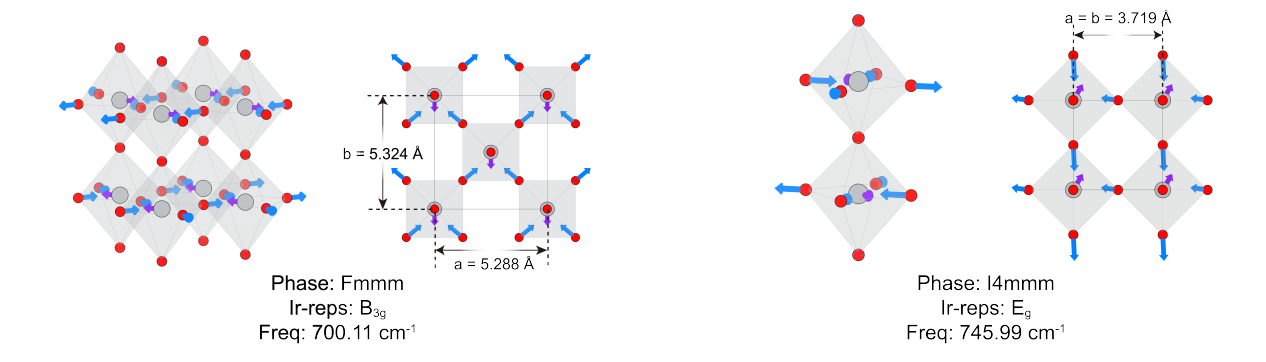


FIG. S5. The corresponding modes found in Fmmm and I4/mmm phases to the major peaks (A7 and A8) in Amam phase with close frequencies and similar vibrational patterns. With ir-reps B_{3g} and E_g the modes are Raman inactive under our experimental setup.

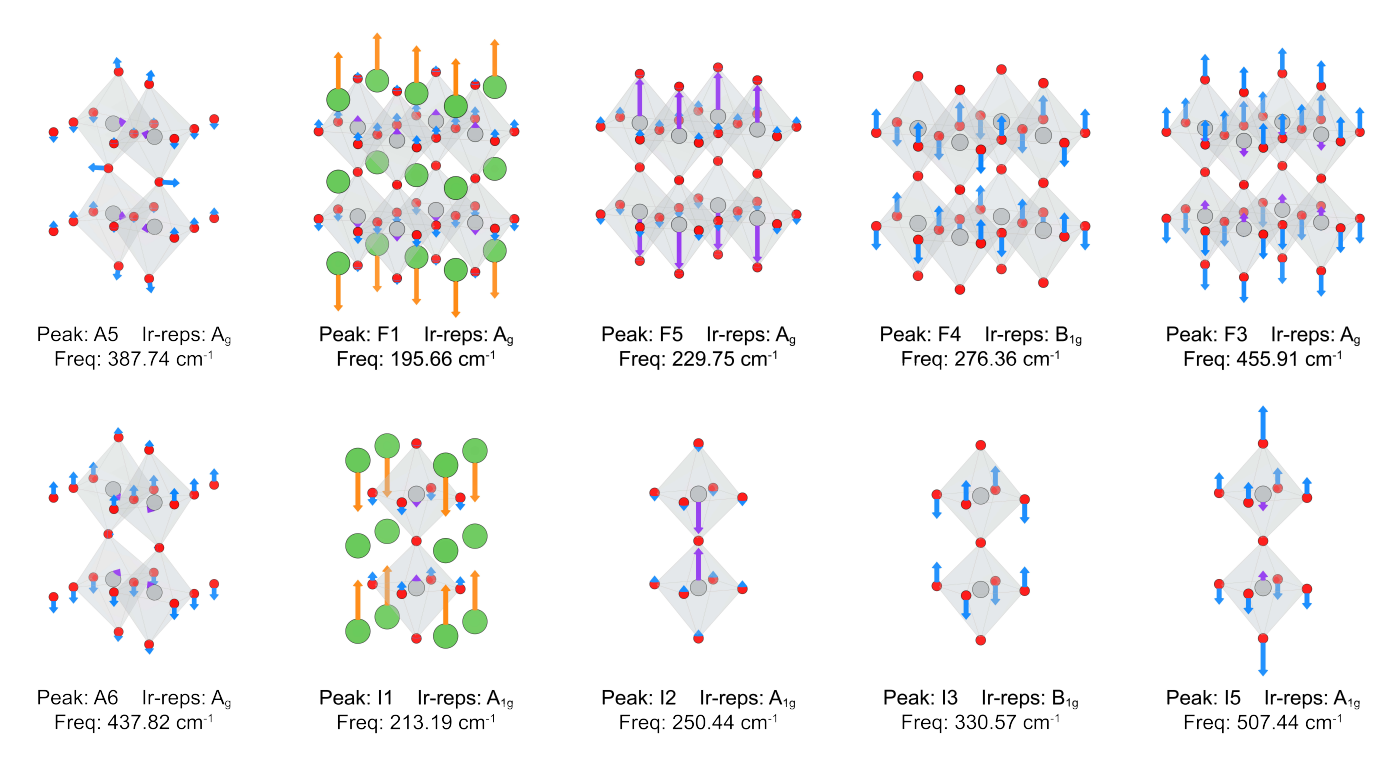


FIG. S6. Visualization of additional phonon modes. The La atoms with notable vibrations are not omitted. Some vectors are rescaled for display.

^[1] P. Borowicz, Depth-sensitive raman investigation of metaloxide-semiconductor structures: Absorption as a tool for variation of exciting light penetration depth, Journal of Spectroscopy **2016**, 1617063 (2016).

^[2] J. Yu, J. L. Sun, X. J. Meng, Z. M. Huang, and Q. Liang, Ultraviolet-infrared optical properties of highly (100)oriented LaNiO₃ thin films on Pt-Ti-SiO₂-Si wafer, Journal of Applied Physics 90, 2699 (2001).

^[3] National Institute of Standards and Technology (NIST), XCOM: Photon cross sections database (2025), accessed on 2025-09-21.

^[4] P. E. Blöchl, Projector augmented-wave method, Phys. Rev. B 50, 17953 (1994).

^[5] E. Kroumova, M. Aroyo, J. Perez-Mato, A. Kirov, C. Capillas, S. Ivantchev, and H. Wondratschek, Bilbao crystallographic server: Useful databases and tools for phase-transition studies, Phase Transitions 76, 155 (2003).